Journal of the Mechanics and Physics of Solids 104 (2017) 157–171

Contents lists available at ScienceDirect

Journal of the Mechanics and Physics of Solids

journal homepage: www.elsevier.com/locate/jmps

Laue micro-diffraction and crystal plasticity finite element simulations to reveal a vein structure in fatigued Cu

A. Irastorza-Landa[a,b], N. Grilli[b,c], H. Van Swygenhoven[a,b,*]

[a] Swiss Light Source (SLS), Paul Scherrer Institut, CH-5232 Villigen PSI, Switzerland
[b] NXMM laboratory, IMX, École Polytechnique Fédérale Lausanne (EPFL), CH-1015 Lausanne, Switzerland
[c] Laboratory for Nuclear Materials (LNM), NES, Paul Scherrer Institut, CH-5232 Villigen PSI, Switzerland

ARTICLE INFO

Article history:
Received 12 July 2016
Revised 1 March 2017
Accepted 18 April 2017
Available online 19 April 2017

Keywords:
Dislocations
Lattice curvatures
X-ray Laue diffraction
Crystal plasticity finite element

ABSTRACT

The formation of a vein during cyclic shearing of a single copper crystal oriented for single slip can be followed in transmission Laue diffraction by analyzing the spatially resolved lattice rotation evolution. Because Laue transmission integrates the signal over the thickness of the sample, the structure of the vein in the beam direction is a priori believed to be inaccessible. Here we show that the vein geometry in the beam direction can be retrieved by comparing lattice curvature tensor components from crystal plasticity finite element simulations with those experimentally derived. Virtual sectional analysis facilitates the interpretation of the measured lattice curvatures of quasi-2D dislocation structures, allowing identifying a vein morphology that is slightly vertically and horizontally inclined in the through thickness direction.

1. Introduction

Dislocations move across the crystal lattice in response to the applied stress and self-organize into defined patterns, determining the macroscopic behavior of the materials (Argon, 2007; Kubin, 2013; Kubin et al., 2002). The developed dislocation arrangements depend on the applied loading conditions and the crystallographic orientation of the crystal. During fatigue at low and intermediate strain amplitudes in single slip oriented copper single crystals, so-called channel-vein dislocation structures are expected, which transform into persistent slip bands (PSBs) after a large number of cycles (Ackermann et al., 1984; Ahmed et al., 2006). Fig. 1 shows the schematic of such a vein-channel structure. The veins consist mainly of edge dipole bundles of primary dislocations that are aligned approximately with the dislocation line perpendicular to the Burger's vector and slip plane normal, and extend in the third dimension. The channels are almost dislocation-free regions, where dislocations travel back and forth during cycles. Veins are reported to have a characteristic width of 1.5 μm in saturation (Laird et al., 1986).

The accumulation of edge dipoles on the primary (111) slip plane with Burgers vectors $[\bar{1}\,0\,1]$ causes rotation about an axis parallel to the $[1\,\bar{2}\,1]$ direction –i.e. the dislocation line direction (Mughrabi, 2006a). A lattice misorientation of 0.33° around the primary edge dislocation line has been reported for a copper single crystal fatigued till PSBs were formed (Mughrabi, 2006b; Wilkens et al., 1980). The misorientation for a vein is expected to be lower (Mughrabi, 2006a). Elec-

* Corresponding author.
E-mail address: helena.vanswygenhoven@psi.ch (H. Van Swygenhoven).

http://dx.doi.org/10.1016/j.jmps.2017.04.010

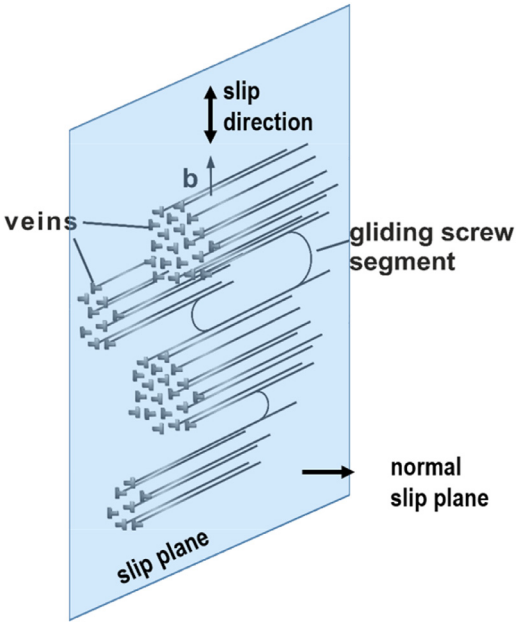

Fig. 1. Schematic of the vein-channel representation.

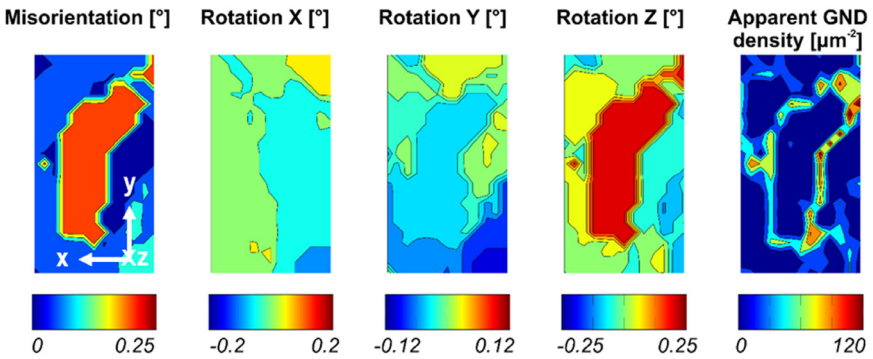

Fig. 2. Misorientation, rotation field and apparent GND density of the developed vein (data obtained from Irastorza-Landa et al., 2016).

tron microscopic observations did not reveal lattice misorientation, but relaxation due to the thin film sample preparation procedure cannot be excluded (Neumann, 1983).

Using x-ray Laue diffraction scans with sub-micron spatial resolution in 2D, the developing microstructure during cyclic shear was followed in a single crystalline copper (Cu) sample (Irastorza-Landa et al., 2016). The experiment was carried out with a miniaturized shear device installed at the MicroXAS beamline of the Swiss Light Source. The Cu single crystal oriented for single slip shaped in Miyauchi's geometry and thinned using picosecond laser ablation to 30 μm (Guitton et al., 2015) was cyclically deformed with different strain amplitudes. Spatial resolved Laue diffraction patterns were recorded in transmission mode after different number of cycles. The evolving dislocation microstructure was analyzed in terms of lattice rotation and apparent geometrically necessary dislocation (GND) densities (Irastorza-Landa et al., 2016). The evolution of the GND traces showed a clear redistribution of the pre-existing GNDs and the appearance of regions surrounded by GND walls with no GNDs inside the perimeter. Such regions were recognized as developing vein structures. Fig. 2 shows the distribution of the misorientation, the rotations about *X*-, *Y*- and *Z*- axes and the apparent GND density of the developed vein (Irastorza-Landa et al., 2016). The vein is rotated predominantly around *Z*-axis by 0.22° and is surrounded with GND walls in its perimeter.

In this experiment, the saturation stage has not been reached and no slip bands, characteristic feature of PSBs (Grosskreutz, 1971), were observed on the surface. Along the dislocation line direction the veins are expected to be curved dislocation structures, as has been observed in TEM images (Basinski et al., 1980; Mughbrabi et al., 1979). Since in Laue micro-diffraction in transmission mode information is integrated along the sample depth, curvatures of the vein structure along the depth of the sample cannot be resolved.

Here we present synergetic work between Laue micro-diffraction experiments and crystal plasticity finite element (CPFE) simulations performed in order to reveal the geometrical structure of the vein responsible for the observed misoriented area in Fig. 2.

2. Methodology

2.1. Lattice curvature from X-ray diffraction data

The Laue diffraction scan with step size of 300 nm covering $10 \times 25\,\mu m^2$ was collected after 120 fully reversed shear fatigue cycles integrated over a thickness of 30 µm. More details about the conducted mechanical test can be found in Irastorza-Landa et al. (2016). Each diffraction pattern is indexed using the maximum intensity for each reflection. The orientation matrix, **G**, is determined using a refinement procedure, after which the relative misorientation between two neighboring points is calculated. This corresponds to the curvature tensor κ_{ij} that is defined as the gradient of the rotation about the '*i*' axis along the '*j*' direction:

$$\kappa_{ij} = \frac{\partial \boldsymbol{\theta}_i}{\partial \mathbf{x}_j} \text{ with } \{i, j\} = \{x, y, z\} \tag{1}$$

where $\boldsymbol{\theta}$ is the lattice rotation vector.

The disorientation vector ($\Delta\boldsymbol{\theta}$) defines the orientation difference between two neighboring points (A and B). In sample coordinates, it can be derived as follows:

$$\Delta\mathbf{G} = \mathbf{G}_A^{-1}\mathbf{G}_B \tag{2}$$

$$\Delta\theta = \arccos\left(\frac{\Delta G_{ii} - 1}{2}\right) \tag{3}$$

with ΔG_{ii} the trace of $\Delta\mathbf{G}$.

$$\Delta\theta_k = -\epsilon_{kij}\Delta G_{ij}\frac{\Delta\theta}{2\sin\Delta\theta} \tag{4}$$

with $\{i, j, k\} = \{x, y, z\}$ and ϵ_{kij} the Levi-Civita permutation symbol.

From the disorientation of two points, separated spatially by a distance $\Delta\mathbf{x}$, the lattice curvatures can be approximated as:

$$\kappa_{ij} \approx \frac{\Delta\theta_i}{\Delta\mathbf{x}_j} \text{ with } \{i, j\} = \{x, y, z\} \tag{5}$$

When working in Laue transmission mode, the differentiation along the third direction is lost. Therefore, only six components of the curvature tensor are available: κ_{ix} and κ_{iy} with $\{i\} = \{x, y, z\}$. A similar procedure has been applied by Pantleon (2008) to obtain lattice curvatures from EBSD measurements. It has also been applied in 3D X-ray diffraction by Larson et al. (2007) for which the full curvature tensor can be obtained.

In the absence of elastic strain or in the assumption of small elastic strains, rotations and/or small elastic strain gradients, the measured lattice curvatures can be related to the GND density by the Nye's formula (Nye, 1953):

$$\boldsymbol{\alpha} \approx \kappa^T - \kappa_{ii}\boldsymbol{I} \tag{6}$$

with κ_{ii} the trace of $\boldsymbol{\kappa}$ and $\boldsymbol{I}$ the identity matrix, which yields:

$$\begin{pmatrix} \alpha_{xx} & \alpha_{xy} & \alpha_{xz} \\ \alpha_{yx} & \alpha_{yy} & \alpha_{yz} \\ \alpha_{zx} & \alpha_{zy} & \alpha_{zz} \end{pmatrix} = \begin{pmatrix} -\kappa_{yy} - \kappa_{zz} & \kappa_{yx} & \kappa_{zx} \\ \kappa_{xy} & -\kappa_{xx} - \kappa_{zz} & \kappa_{zy} \\ \kappa_{xz} & \kappa_{yz} & -\kappa_{xx} - \kappa_{yy} \end{pmatrix} \tag{7}$$

In our experiment only six components of the curvature tensor are available (κ_{ix} and κ_{iy} with $\{i\} = \{x, y, z\}$) - marked in blue. This allows to determine an apparent density of GNDs as suggested in Gupta and Agnew (2010):

$$\rho_{\text{apparent}} = \frac{1}{b}(|\alpha_{xy}| + |\alpha_{xz}| + |\alpha_{yx}| + |\alpha_{yz}| + |\alpha_{zz}|) \tag{8}$$

2.2. Computational model

The simulations are based on the CPFE method and dislocation based constitutive laws. They are carried out using the DAMASK subroutine – Düsseldorf Advanced Material Simulation Kit (Roters et al., 2012). The CPFE method is formulated using finite strains and the deformation gradient $\boldsymbol{F}$ is multiplicatively decomposed into an elastic and a plastic component (Lee, 1969):

$$\boldsymbol{F} = \boldsymbol{F}_e\boldsymbol{F}_p \tag{9}$$

The elastic deformation gradient is related to the stress by an anisotropic elastic stiffness tensor $\boldsymbol{C}$:

$$\boldsymbol{S} = \boldsymbol{C} \cdot (\boldsymbol{F}^T{}_e\boldsymbol{F}_e - \boldsymbol{I})/2 \tag{10}$$

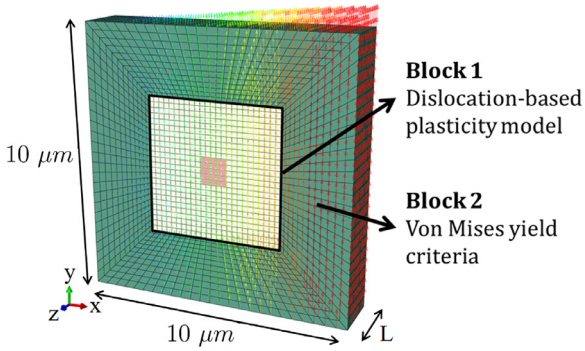

Fig. 3. Representative volume of the simulation and boundary condition.

In FCC materials the elastic stiffness tensor is characterized by three elastic constants c_{11}, c_{12}, c_{44} (Overton and Gaffney, 1955). The time evolution of the plastic deformation gradient depends on $\boldsymbol{L}_p$, which is the so-called plastic velocity gradient (Roters et al., 2010). In the CPFE method, $\boldsymbol{L}_p$ has contributions from the shear rates ($\dot{\gamma}^{\alpha}$) of all the slip systems:

$$\boldsymbol{L}_p = \sum_{\alpha=1}^{12} \dot{\gamma}^{\alpha} \boldsymbol{m}^{\alpha} \otimes \mathbf{n}^{\alpha} \tag{11}$$

where the unit vectors $\boldsymbol{m}^{\alpha}$ and $\mathbf{n}^{\alpha}$ describe the slip direction and the normal to the slip plane of the slip system α.

The simulated geometry consists of two regions, as schematically shown in Fig. 3. A dislocation-based constitutive model is used in the central part (white region). This parallelepiped with dimensions $5 \times 5 \times \mathrm{L}\,\mu\mathrm{m}^3$ will be called "Block 1" and it is embedded in a region "Block 2" with dimensions $10 \times 10 \times \mathrm{L}\,\mu\mathrm{m}^3$.

The model applied (Grilli et al., 2015) in Block 1 uses positive and negative edge and screw dislocations as state variables. It incorporates dislocation multiplication, annihilation and cross slip. The dislocation motion through the geometry is described by flux terms (Roters et al., 2010) and the threshold resolved shear stress to move a dislocation on the slip system α is (Arsenlis and Parks, 2002):

$$\tau_{th}^{\alpha} = \mu b \sqrt{\sum_{\beta=1}^{12} \xi^{\alpha\beta} \rho^{\beta}} \tag{12}$$

where μ is the shear modulus, b is the Burgers vector, $\xi^{\alpha\beta}$ are interaction coefficients among the slip planes and ρ^{β} the total dislocation density on the slip system β.

A cluster of immobile dislocations is introduced in Block 1 to mimic the presence of a vein, schematically represented by the pink square in the white region in Fig. 3. Different configurations for the immobile dislocation cluster are used, as explained in Section 4. During simulation of a fatigue cycle, mobile dislocations will accumulate at the interface of the cluster when the threshold stress in Eq. (12) is reached and will form dislocation walls constituted of GNDs. Periodic dislocation fluxes are imposed in 3D on the boundary of Block 1 to avoid size effects. Shear displacement is applied on the right surface of Block 2. The obtained displacement field is shown by the arrows in Fig. 3.

The boundary region Block 2 is described using Von Mises plasticity (Peirce et al., 1982). The plastic velocity gradient is:

$$\boldsymbol{L}_p = \sqrt{\frac{2}{3}} \dot{\gamma}_0 \frac{\|\boldsymbol{S}^*\|^{n-1}}{g^n} \boldsymbol{S}^* \tag{13}$$

where $\dot{\gamma}_0$ is a reference shear strain rate, g is the flow stress, n is the stress exponent, $\boldsymbol{S}^*$ is the deviatoric stress and $\|\boldsymbol{S}^*\|$ its second invariant. The flow stress evolves from g_o to g_{sat} as:

$$\dot{g} = h_0 \dot{\gamma}_0 \left(\frac{\|\boldsymbol{S}^*\|^n}{g^n} \right) \left| 1 - \frac{g}{g_{sat}} \right|^a \tag{14}$$

Pure copper single crystal parameters from Déprés et al. (2008) and Overton and Gaffney (1955) have been used and they are reported in Table 1.

The CPFE method can calculate the lattice rotation by left polar decomposition of the elastic deformation gradient (Eberl et al., 2002) as:

$$\boldsymbol{F}_e = \boldsymbol{G} \cdot \boldsymbol{U}_e \tag{15}$$

where $\boldsymbol{G}$ is a rotation matrix, analogue to experimental, and $\boldsymbol{U}_e$ represents pure stretching. Therefore, the same procedure as explained in the experimental Section 2.1 can be followed to calculate the rotation fields, lattice curvatures and apparent GND density. The rotation at each (x,y) point is the averaged rotation along the Z-axis Fig. 3.

Table 1
Material parameters used for simulations.

Elastic constants	c_{11}	165.00	GPa
	c_{12}	117.52	GPa
	c_{44}	75.68	GPa
Stress exponent	n	20	
Initial value of slip resistance parameter	g_o	10	MPa
Saturation value of slip resistance parameter	g_{sat}	28	MPa
Reference shear strain rate	$\dot{\gamma}_0$	$1 \cdot 10^{-10}$	s^{-1}
Hardening parameters	a	1	
	h_o	100	MPa

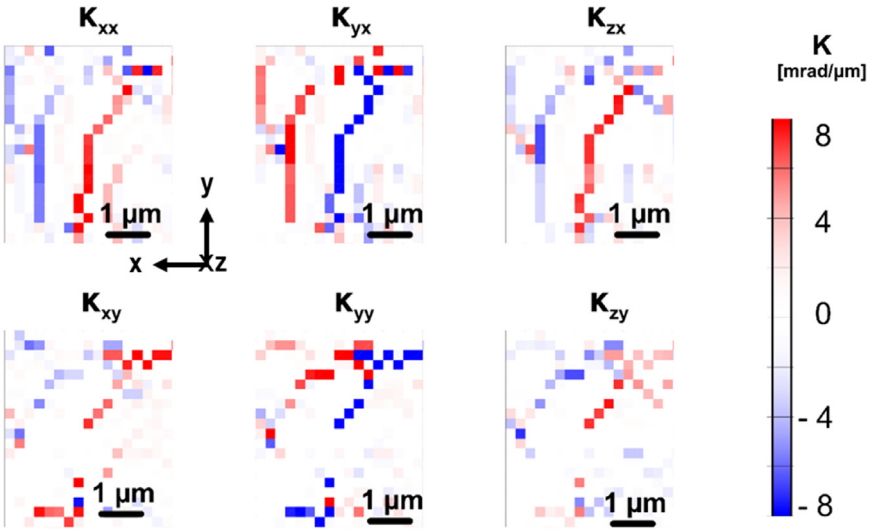

Fig. 4. Experimental lattice curvatures of the evolved misoriented region.

3. Experimental lattice curvatures

Fig. 4 shows the lattice curvature components of the evolved region in mrad/μm. For comparison, the same scale bar (|8 mrad/μm|) has been given to all the components. At the left wall of the rotated area, the region has negative torsion around *X*-axis (κ_{xx}), a plane perpendicular to *X*-axis has positive flexion around the *Y*-axis (κ_{yx}) and negative around *Z*-axis (κ_{zx}). Reverse signs are found at the right wall. On the upper side, the region has positive torsion around *Y*-axis (κ_{yy}) and the plane perpendicular to the *Y*-axis has negative flexion around both *X*-axis (κ_{xy}) and *Z*-axis (κ_{zy}). The lower part is characterized by opposite values. The geometrical meaning of the lattice curvatures is summarized in Fig. 5.

The statistical distribution of each lattice curvature is graphically depicted as boxplots in Fig. 6. Briefly, each box represents the middle fifty (interquartile = IQR) of the population and the whiskers extend till |1.5 × IQR|. The points plotted as '+' symbols, outliers, are values lying outside the |1.5 × IQR| range. The medians of all distributions, the central mark of the box, correspond to ~0 mrad/μm. Detailed information of boxplots is given in Appendix A. The boxplot shows that outliers of κ_{xx}, κ_{yx} and κ_{yy} exceed |10 mrad/μm|, whereas the limits of κ_{xy}, κ_{zx} and κ_{zy} are below |10 mrad/μm|. Out of 378 total measurements, 47–49% are outliers.

Dislocations corresponding to the primary slip system for single slip orientation have their Burgers vector parallel to $Y = [\bar{1}01]$ and line direction in the *Z*-axis. If straight, these dislocations should cause only non-zero values for κ_{zx} and κ_{zy} lattice curvatures (see Appendix B). Therefore, κ_{zx} and κ_{zy} can be directly attributed to the presence of primary edge GND walls surrounding the dipoles, as schematically drawn in Fig. 7. Nevertheless, the experimental measurements show that κ_{zx} and κ_{zy} are not the only present lattice curvatures. In fact, their distribution can be narrower when comparing to the distribution of other curvature components (see Fig. 6). In order to understand this observation computational simulations with different vein geometries have been performed.

4. Simulated geometries

Four configurations representing possible geometries that dislocations could adopt when forming a vein have been introduced in Block 1 shown in Fig. 3:

- A straight vein

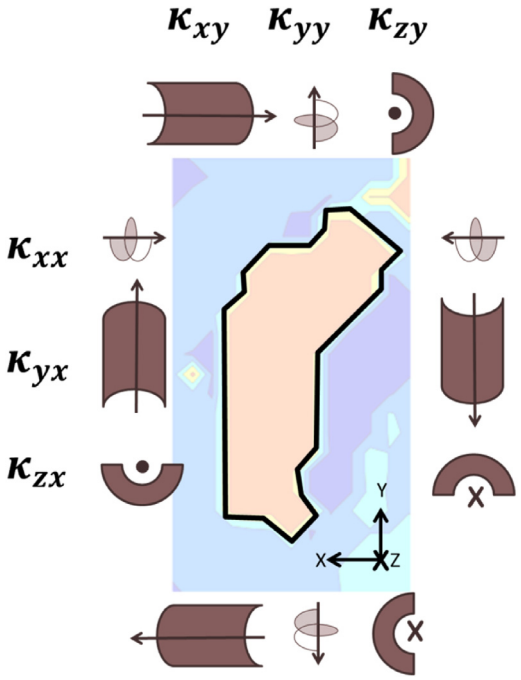

Fig. 5. Representation of the observed lattice curvatures around the region. See text for description.

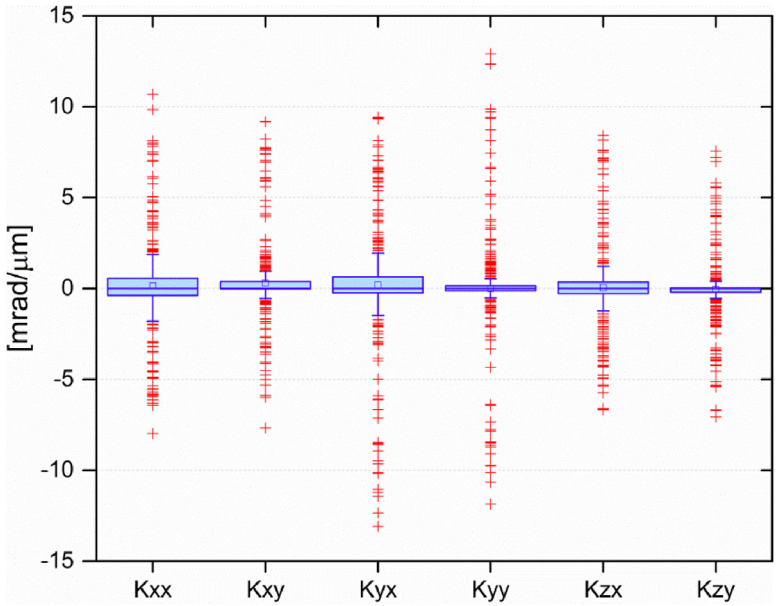

Fig. 6. Statistical distribution of the experimental lattice curvatures. Blue box represents the IQR of the population, the whiskers extend till |1.5 × IQR|and the red '+' are outliers. (For interpretation of the references to color in this figure legend, the reader is referred to the web version of this article.)

- A vein inclined towards the *Y*-axis (*Y*-inclined vein)
- A vein inclined towards the *Y*- and the *X*-axis (*Y* & *X*-inclined vein)
- Two veins, both inclined towards the *Y*-axis (Two inclined veins)

The schematic and geometrical details are shown in Fig. 8.

Each simulated vein has a density of 100 μm^{-2} immobile dislocations. Additionally, a uniform mobile dislocation density of 5 μm^{-2} for each dislocation type (positive and negative, edge and screw dislocations) is added in Block 1. 1% random perturbations are added to this uniform distribution and these fluctuations have the same magnitude for positive and negative signed mobile dislocations. Each vein configuration is then subjected to one full cycle with an applied shear strain of

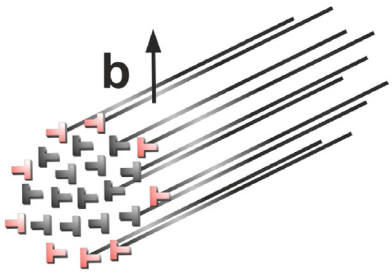

Fig. 7. Schematic of dislocations forming dipoles in a vein. Excess of dislocations around the vein (in red) contribute to GNDs. (For interpretation of the references to color in this figure legend, the reader is referred to the web version of this article.)

		Straight vein	Y-inclined vein	Y&X-inclined vein	Two inclined veins
		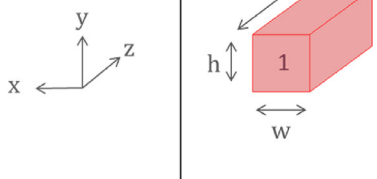	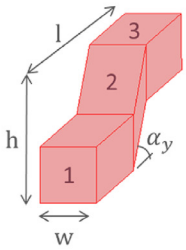	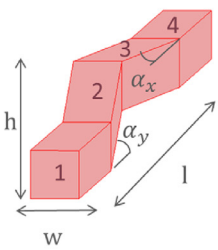	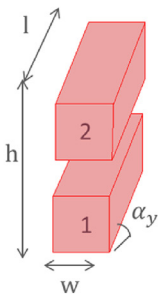
Dimensions	**Total height (h)**	1 μm	2 μm	2 μm	4 μm
	Height of each cuboid	h_1= 1 μm	h_1= 1 μm h_2= 2 μm h_3= 1 μm	h_1= 1 μm h_2= 2 μm h_3= 1 μm h_4= 1 μm	h_1= 2 μm h_2= 2 μm
	Total width (w)	1μm	1 μm	2 μm	1μm
	Width of each cuboid	w_1= 1 μm	w_1= 1 μm w_2= 1 μm w_3= 1 μm	w_1= 1 μm w_2= 1 μm w_3= 2 μm w_4= 1 μm	w_1= 1 μm w_2= 1 μm
	Total length (l)	1 μm	1 μm	1.5 μm	2 μm
	Length of each cuboid	l_1= 1 μm	l_1= 0.375 μm l_2= 0.250 μm l_3= 0.375 μm	l_1= 0.375 μm l_2= 0.250 μm l_3= 0.375 μm l_4= 0.500 μm	l_1= 2 μm l_2= 2 μm
	Y-inclination (α_y)	-	76°	76°	26.5°
	X-inclination (α_y)	-	-	69°	-

Fig. 8. Schematic and geometrical details of simulated veins.

~0.50%, during which primary dislocations are trapped around the immobile vein as schematically shown in Fig. 7. The rotation field of each configuration is then calculated as explained in Section 2.2. As reference, the rotation field after one full cycle is calculated for a configuration without an immobile dislocation cluster. This rotation field is subtracted from those obtained with immobile clusters to remove boundary effects caused by the interface between Block 1 and Block 2.

5. Simulated rotation field, apparent density of GNDs and lattice curvatures

Fig. 9 shows the rotation about the *Z*-axis [mdeg] and the apparent GND density [μm^{-2}] distributions for the different vein geometries. All of them show positive rotation about the *Z*-axis. The value of the *Z*-rotation is higher for the straight vein than for the two inclined clusters. The *Y*-inclined and *Y* & *X*- inclined veins have intermediate rotation values. Interestingly, the apparent GND density maps show that an inclination across the thickness is necessary in order to have apparent

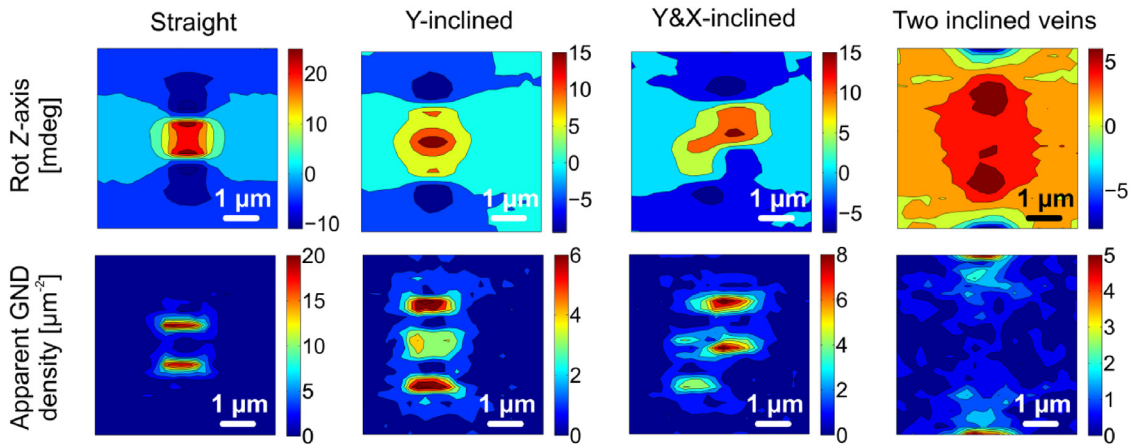

Fig. 9. (a) Rotation about *Z*-axis and (b) Apparent GND density of different simulated vein geometries.

GNDs in the lateral walls. A pure straight configuration would create only apparent GND densities at the top and bottom of the vein. In the special case of two inclined clusters, the apparent GND density has no clear structure.

The statistical distributions of each lattice curvature component are graphically depicted as boxplots in Fig. 10 for all simulated vein configurations. It can be observed that the distributions of κ_{xx}, κ_{xy}, κ_{yx} and κ_{yy} are very similar in all the geometries: the values are slightly higher in the *Y*-inclined case than in the other configurations. On the other hand, κ_{zx} and κ_{zy} are extremely sensitive to the vein configuration. Their outlier values are highly influenced (at least a factor of two) when changing the geometry from straight to any of the other three configurations. These results can explain why experimentally the expected κ_{zx} and κ_{zy} do not have the highest values.

6. Curvatures from a *Y* & *X*-inclined vein and sectional analysis

The lattice curvatures for the *Y* & *X*-inclined vein are further analyzed. In order to have more pronounced rotation fields, a longer vein is simulated with similar geometrical configurations as shown in Fig. 11. The vein can be divided in four sections/cuboid, each one 1 μm long. The first section is straight along the *Z*-axis, Section 2 is inclined along *Y*-axis, Section 3 is inclined in *X*-axis and the last section is again straight along the *Z*-axis.

Fig. 12 shows the distribution maps of each lattice curvature component for the *Y&X*-inclined long vein configuration derived from averaged rotation fields integrated over the entire thickness (see Appendix C for average rotation fields). In the right side of each box a schematic of the lattice curvatures is shown. One can observe several similarities when comparing the simulated and experimental distributions shown in Fig. 4:

- Simulated κ_{xx} and κ_{zx} components have vertical boundaries in the lateral walls of the vein. Similar to experimental results, the signs are reversed in the left and right walls. The distribution of the κ_{yx} component is not as defined as the one of κ_{xx} and κ_{zx} components, but faint left and right walls can be distinguished. The sign is, however, reversed comparing to experimental values. This is related to the average *Y*- rotation field obtained (Appendix C) and is discussed below.
- Simulated κ_{xy} and κ_{zy} components have horizontal boundaries in the upper and lower walls of the vein. The signs are reversed in the upper and lower walls, and the signs match when comparing to experimental results. The distribution of κ_{yy} also shows reversed signs in the upper and lower walls but the sign and distribution do not have strong correlation with the experimental observations.

The influence of the geometry of each cuboid of the long *Y&X*-inclined vein shown in Fig. 11 is now studied in detail by calculating the lattice curvatures of the sections separately. Fig. 13 shows the sectional maps of all lattice curvature components and Fig. 14 shows their distribution as boxplots. The sectional rotation distributions are given in Appendix C.

One can observe that in all sections the simulated κ_{zx} and κ_{zy} show localized traces forming the left-right walls or upper-lower walls of the vein with same sign as in experiments. The values are rather similar in all sections and they are higher compared to the other lattice curvatures. The greatest variation is observed in Section 3 where the values of κ_{zx} double those of the other sections. This corresponds to the part where the vein is inclined along *X*-axis and the *X*- and *Z*-rotation are the highest (see Appendix C).

When analyzing the maps of the other four components κ_{xx}, κ_{xy}, κ_{yx} and κ_{yy}, it is found that the distribution of the lattice curvatures is different for each cuboid:

- There is no standard structure of κ_{xx} in the straight sections (1 and 4) where the vein is located: in Section 1, for instance, the inner part of the vein has positive κ_{xx} values surrounded by negative values outside the vein; in Section 4

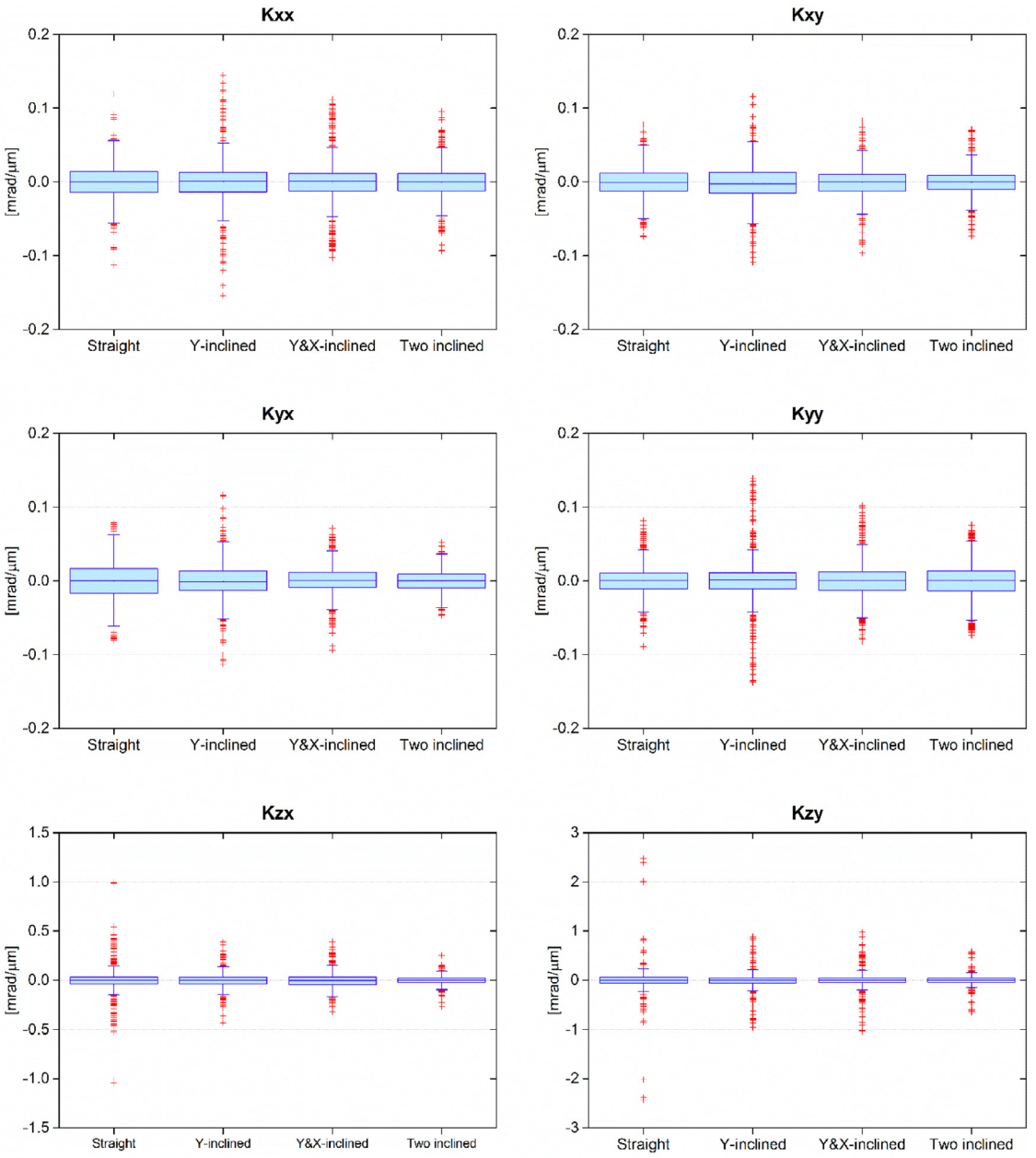

Fig. 10. Lattice curvature components distributions of the four computed vein geometries.

the left and right walls have negative and positive κ_{xx} values respectively. In the *Y*-inclined Section 2, the κ_{xx} traces are mainly in the upper and lower walls due to the gradient induced by the inclination. In the *X*-inclined Section 3, the lattice curvature is only localized in the left and right walls, and the values are highest. Besides they match in sign with those measured experimentally: left negative, right positive. Therefore Section 3 resembles more the experimental data.

- In Sections 1, 3 and 4, κ_{xy} mark the upper and lower walls of the vein. The signs are in agreement with experimental observations. The κ_{xy} values are highest in Section 3, similar as what was observed for κ_{xx}. In the *Y*-inclined Section 2, the κ_{xy} traces are localized in the left-right walls of the vein due to the gradient induced by the inclination.
- κ_{yx} shows similar values for all four sections. In the straight sections (1 and 4) there is no defined structure where the vein is located. In the *Y*-inclined Section 2, the κ_{yx} traces are located in the left-right walls similar to those observed experimentally and with the same signs. In the *X*-inclined Section 3, on the other hand, the κ_{yx} traces mark the upper-lower walls of the vein. This difference is induced by the particular inclination in each section, a piece of informa-

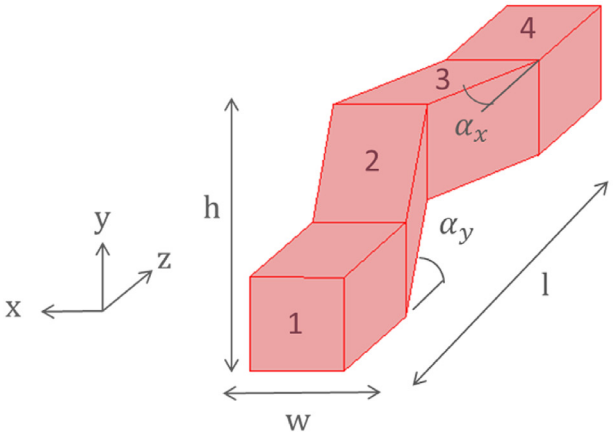

Dimensions of long Y&X-inclined vein	
Projected height (h)	2 μm
Height of each cuboid	h_1= 1 μm h_2= 2 μm h_3= 1 μm h_4= 1 μm
Projected width (w)	2 μm
Width of each cuboid	w_1= 1 μm w_2= 1 μm w_3= 2 μm w_4= 1 μm
Projected length (l)	4 μm
Length of each cuboid	l_1= 1 μm l_2= 1 μm l_3= 1 μm l_4= 1 μm
Y-inclination (α_y)	45°
X-inclination (α_y)	45°

Fig. 11. Schematic and geometrical details of long *Y&X*-inclined vein configuration.

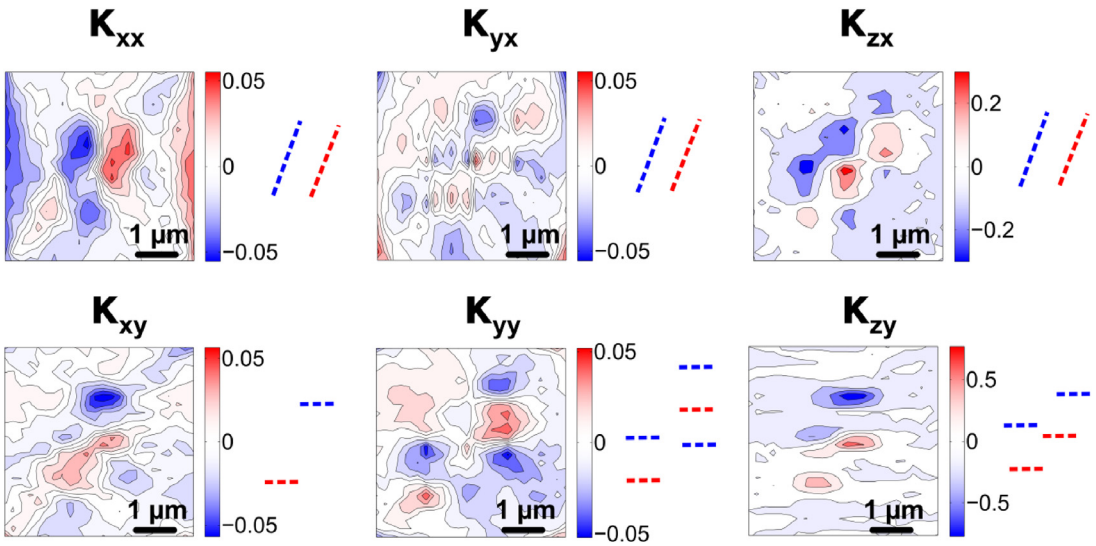

Fig. 12. Distribution of lattice curvature components of the simulated *Y* & *X*-inclined long vein in [mrad/μm].

tion that is lost when analyzing the averaged lattice curvature distribution. This causes the dissimilarities between the experimental and averaged computed lattice curvature maps (see Fig. 12).

- The κ_{yy} traces in the straight sections (1 and 4) and in the *X*-inclined Section 3 have non-zero values in the left-right walls. Their values are however lower when comparing to those of *Y*-inclined Section 2. There, the κ_{yy} traces mark the upper-lower walls analogue to the experimental data, and they have same sign. Similar as for κ_{yx}, this information is lost in the averaged plots shown in Fig. 12.

In summary, the sectional analysis of the vein reveals that vertical and horizontal inclinations are required to explain the experimentally obtained lattice curvature distributions.

7. Conclusions

Lattice curvatures in relation to a vein formed during cyclic fatigue in a single Cu crystal oriented for single slip have been derived from spatially resolved Laue micro-diffraction in transmission mode. Since Laue in transmission cannot provide information on the distribution of lattice curvatures along the depth of the sample, dedicated CPFE simulations are performed in order to obtain information on the geometry of the vein. The dedicated simulation brings detailed information on the lattice curvature caused by a straight dislocation vein and allows differentiation between veins with different inclined sections. By comparing with experimentally obtained lattice curvatures measured for a vein structure, it is possible to geometrically interpret the vein in the 3rd dimension. In particular, for a cyclic fatigued single slip oriented Cu crystal,

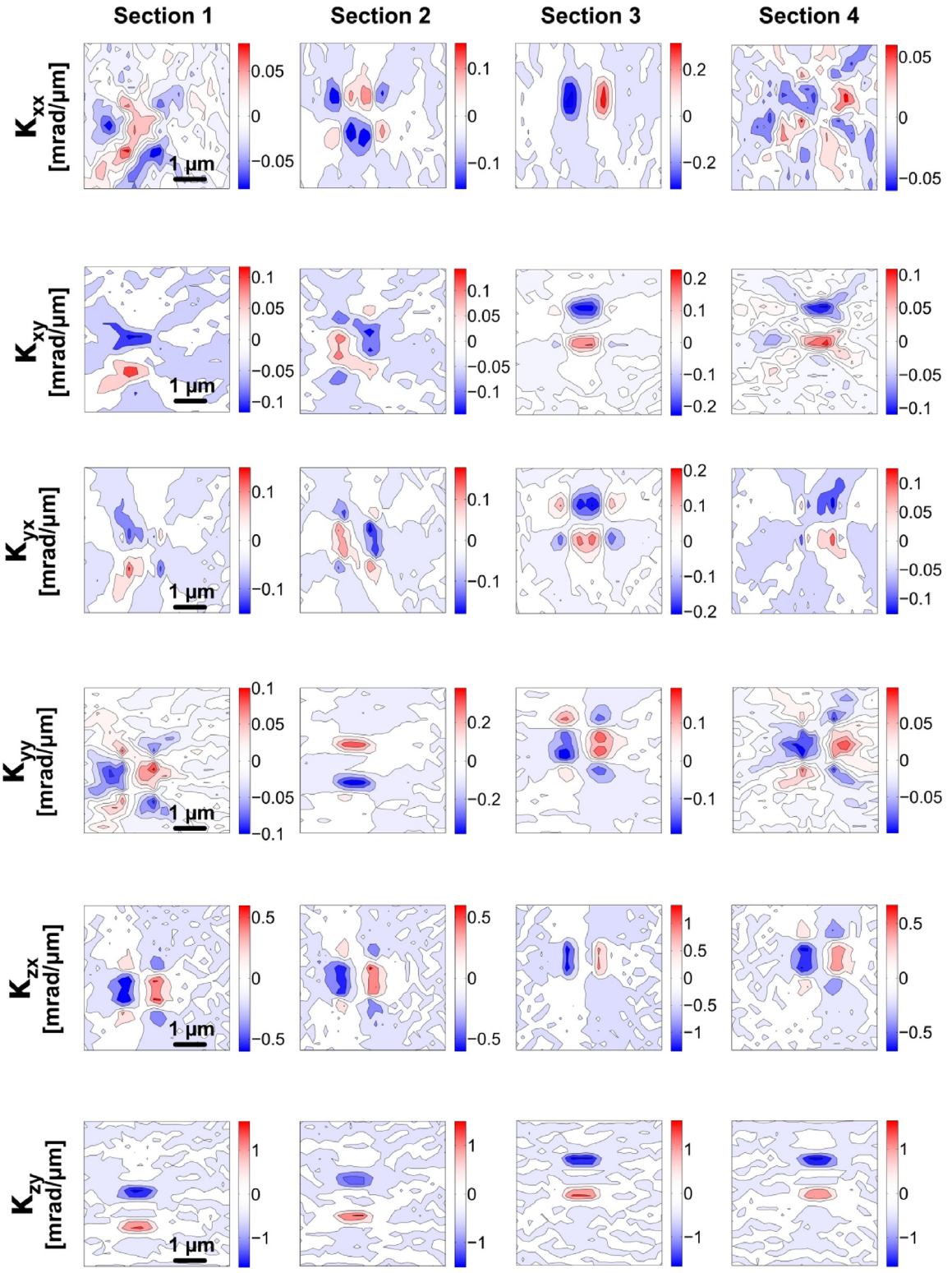

Fig. 13. Sectional lattice curvature maps of a *Y-X*-inclined long vein.

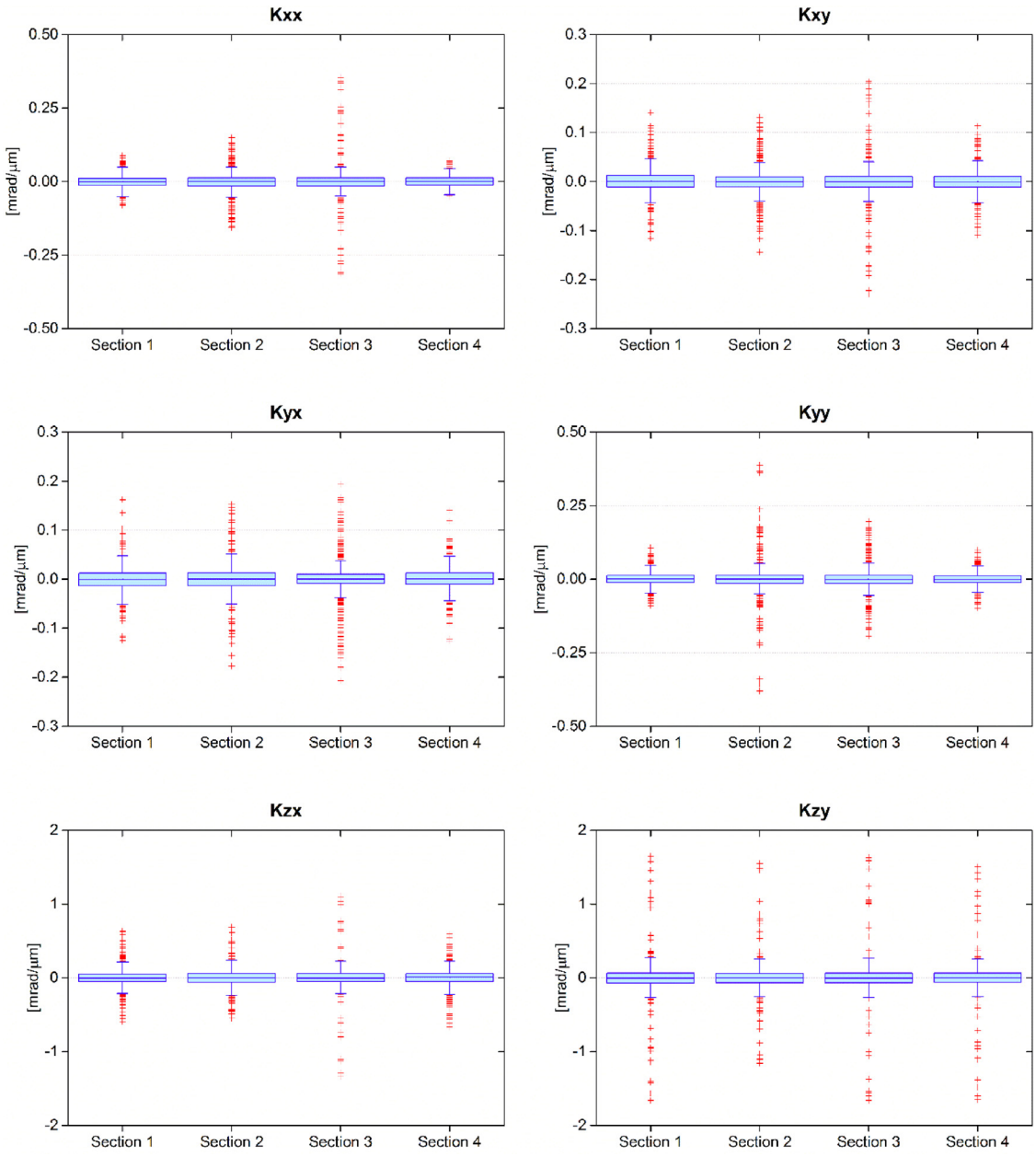

Fig. 14. Lattice curvature components distributions at each section of a *Y-X*-inclined long vein.

the developing vein is slightly inclined vertically and horizontally in the third direction. This is in good agreement with the curved dislocation structures observed in TEM images such as in Basinski et al. (1980) and Mughbrabi et al. (1979).

Acknowledgments

The authors thank the Swiss National Science foundation for financial support (SNF – 138240). A.I-L and H.V.S. thank the European Research Council for the advanced grant MULTIAX (339245).

Appendix A. Statistical representation of data as boxplots

The box plot is a quick way of examining one or more sets of data graphically. Each box represents the middle fifty of the population. The tops and bottoms of each box are the 25th and 75th percentiles of the samples, respectively. The total length of the box is the interquartile range (IQR). The whiskers, in other words the arms, extend till 1.5 × IQR. The line inside

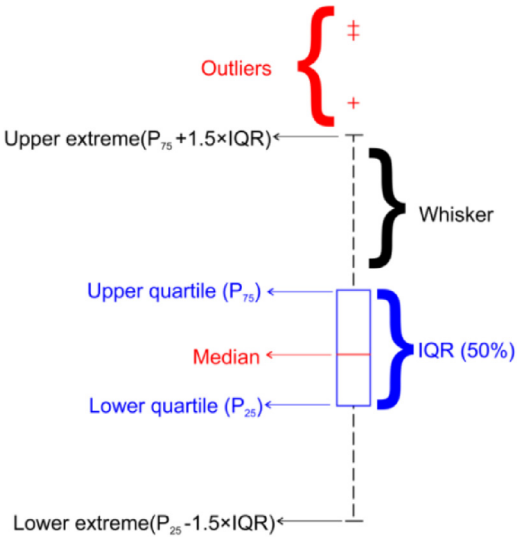

Fig. A.1. Visual representation of a boxplot. Adapted from Mathworks Website (n.d.).

the box is the sample median. The points plotted as '+' symbol are outliers that are values outside the |1.5*IQR| range. The maximum and minimum outlier defines the total range of the distribution. The visual representation of a boxplot is given in Fig. A.1.

Appendix B. Lattice curvatures of infinite edge dislocation with its line along *Z*-axis

The curvature tensor κ_{ij} describes the relative misorientation and is defined as the gradient of the rotation about the '*i*' axis along the '*j*' direction:

$$\kappa_{ij} = \frac{\partial \boldsymbol{\theta}_i}{\partial \mathbf{x}_j} \text{ with } \{i, j\} = \{x, y, k\} \tag{B.1}$$

where $\boldsymbol{\theta}$ is the lattice rotation vector:

$$\theta_k = -\frac{\in_{kij}\omega_{ij}}{2} \text{ with } \{i, j, k\} = \{x, y, z\} \tag{B.2}$$

and where $\boldsymbol{\omega}$ is the lattice rotation tensor (Pantleon, 2008).

This yields:

$$\theta_x = \omega_{zy} \tag{B.3}$$

$$\theta_y = \omega_{xz} \tag{B.4}$$

$$\theta_z = \omega_{yx} \tag{B.5}$$

The lattice rotation field is defined as:

$$\omega_{ij} = \frac{1}{2}\left(\frac{\partial u_i}{\partial x_j} - \frac{\partial u_j}{\partial x_i}\right) \text{ with } \{i, j\} = \{x, y, k\} \tag{B.6}$$

where u is the elastic distortion field (Acharya and Knops, 2013).

The elastic distortion field of a straight dislocation in an infinitely extended isotropic body with the dislocation line along the *Z*- axis is as follows (deWit, 1973):

$$u_x = b_x\left[\frac{\varphi}{2\pi} + \frac{x_x x_y}{4\pi(1-\nu)\rho^2}\right] + \frac{b_y}{4\pi(1-\nu)}\left[(1-2\nu)\ln\rho + \frac{x_y^2}{\rho^2}\right] \tag{B.7}$$

$$u_y = -\frac{b_x}{4\pi(1-\nu)}\left[(1-2\nu)\ln\rho + \frac{x_{yx}^2}{\rho^2}\right] + b_y\left[\frac{\varphi}{2\pi} + \frac{x_x x_y}{4\pi(1-\nu)\rho^2}\right] \tag{B.8}$$

$$u_z = \frac{b_z\varphi}{2\pi} \tag{B.9}$$

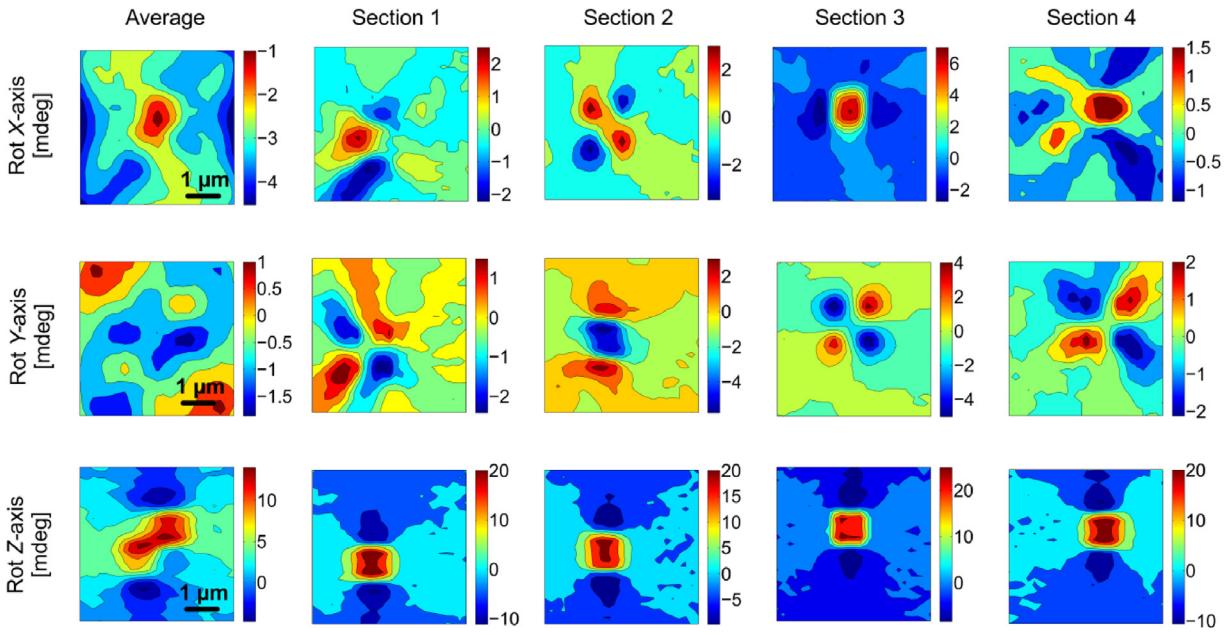

Fig. C.1. Average and sectional rotation fields of the *Y* & *X*-inclined long vein shown in Fig. 11.

where

$$\rho = \sqrt{x_x^2 + x_y^2} \tag{B.10}$$

$$\varphi = \tan^{-1}\left(\frac{x_y}{x_x}\right) \tag{B.11}$$

Now, computing:

$$\omega_{zy} = \frac{1}{2}\left(\frac{\partial u_z}{\partial x_y} - \frac{\partial u_y}{\partial x_z}\right) = 0 \tag{B.12}$$

$$\omega_{xz} = \frac{1}{2}\left(\frac{\partial u_x}{\partial x_z} - \frac{\partial u_z}{\partial x_x}\right) = 0 \tag{B.13}$$

$$\omega_{yx} = \frac{1}{2}\left(\frac{\partial u_y}{\partial x_x} - \frac{\partial u_x}{\partial x_y}\right) \neq 0 \tag{B.14}$$

This yields to the fact that $\theta_z(x, y)$ is the only non-zero component and therefore κ_{zx} and κ_{zy} are the only lattice curvatures induced by an infinite edge dislocation with its line along *Z*-axis.

Appendix C. Average and sectional rotation fields of long *Y&X*-inclined long vein

Fig. C.1.

References

Acharya, A., Knops, R.J., 2013. An observation on the experimental measurement of dislocation density. ArXiv13010869 Cond-Mat.
Ackermann, F., Kubin, L.P., Lepinoux, J., Mughrabi, H., 1984. The dependence of dislocation microstructure on plastic strain amplitude in cyclically strained copper single crystals. Acta Metall. 32, 715–725. doi:10.1016/0001-6160(84)90145-7.
Ahmed, J., Roberts, S.G., Wilkinson, A.J., 2006. Characterizing dislocation structure evolution during cyclic deformation using electron channelling contrast imaging. Philos. Mag. 86, 4965–4981. doi:10.1080/14786430600710941.
Argon, A., 2007. Strengthening Mechanisms in Crystal Plasticity. Oxford University Press.
Arsenlis, A., Parks, D.M., 2002. Modeling the evolution of crystallographic dislocation density in crystal plasticity. J. Mech. Phys. Solids 50, 1979–2009. doi:10.1016/S0022-5096(01)00134-X.
Basinski, Z.S., Korbel, A.S., Basinski, S.J., 1980. The temperature dependence of the saturation stress and dislocation substructure in fatigued copper single crystals. Acta Metall. 28, 191–207. doi:10.1016/0001-6160(80)90068-1.
Déprés, C., Fivel, M., Tabourot, L., 2008. A dislocation-based model for low-amplitude fatigue behaviour of face-centred cubic single crystals. Scr. Mater. 58, 1086–1089. doi:10.1016/j.scriptamat.2008.02.027.
deWit, R., 1973. Theory of disclinations: IV. Straight disclinations. J. Res. Natl. Bur. Stand. Sect. Phys. Chem. 77A, 607. doi:10.6028/jres.077A.036.

Eberl, F., Forest, S., Cailletaud, G., Wroblewski, T., Lebrun, J.L., 2002. Finite-element calculations of the lattice rotation field of a tensile-loaded nickel-based alloy multicrystal and comparison with topographical X-ray diffraction measurements. Metall. Mater. Trans. A 33, 2825–2833. doi:10.1007/s11661-002-0268-1.

Grilli, N., Janssens, K.G.F., Van Swygenhoven, H., 2015. Crystal plasticity finite element modelling of low cycle fatigue in fcc metals. J. Mech. Phys. Solids 84, 424–435. doi:10.1016/j.jmps.2015.08.007.

Grosskreutz, J.C., 1971. The mechanisms of metal fatigue (I). Phys. Status Solidi B 47, 11–31. doi:10.1002/pssb.2220470102.

Guitton, A., Irastorza-Landa, A., Broennimann, R., Grolimund, D., Van Petegem, S., Van Swygenhoven, H., 2015. Picosecond pulsed laser for microscale sample preparation. Mater. Lett. 160, 589–591. doi:10.1016/j.matlet.2015.06.119.

Gupta, V.K., Agnew, S.R., 2010. A simple algorithm to eliminate ambiguities in EBSD orientation map visualization and analyses: application to fatigue crack-tips/wakes in aluminum alloys. Microsc. Microanal. 16, 831–841. doi:10.1017/S1431927610093992.

Irastorza-Landa, A., Van Swygenhoven, H., Van Petegem, S., Grilli, N., Bollhalder, A., Brandstetter, S., Grolimund, D., 2016. Following dislocation patterning during fatigue. Acta Mater. 112, 184–193. doi:10.1016/j.actamat.2016.04.011.

Kubin, L., 2013. Dislocations, Mesoscale Simulations and Plastic Flow. Oxford University Press.

Kubin, L.P., Fressengeas, C., Ananthakrishna, G., 2002. Chapter 57 collective behaviour of dislocations in plasticity. In: Nabarro, F.R.N., Duesbery, M.S. (Eds.), Dislocations in Solids. Elsevier, pp. 101–192.

Laird, C., Charsley, P., Mughrabi, H., 1986. Proceedings of the International Conference on Low Energy Dislocation Structures. Mater. Sci. Eng. 81, 433–450. doi:10.1016/0025-5416(86)90281-8.

Larson, B.C., El-Azab, A., Yang, W., Tischler, J.Z., Liu, W., Ice, G.E., 2007. Experimental characterization of the mesoscale dislocation density tensor. Philos. Mag. 87, 1327–1347. doi:10.1080/14786430600943930.

Lee, E.H., 1969. Elastic-plastic deformation at finite strains. J. Appl. Mech. 36, 1. doi:10.1115/1.3564580.

Mathworks Website, n.d. Box plot - MATLAB boxplot - http://ch.mathworks.com/help/stats/boxplot.html [WWW Document]. Boxplot. URL http://ch.mathworks.com/help/stats/boxplot.html (accessed 5.22.16).

Mughbrabi, H., Ackermann, F., Herz, K., 1979. Persistent slipbands in fatigued face-centered and body-centered cubic metals. In: Fong, J. (Ed.), Fatigue Mechanisms. ASTM International, 100 Barr Harbor Drive, PO Box C700, West Conshohocken, PA 19428-2959 69-69–37.

Mughrabi, H., 2006a. Deformation-induced long-range internal stresses and lattice plane misorientations and the role of geometrically necessary dislocations. Philos. Mag. 86, 4037–4054. doi:10.1080/14786430500509054.

Mughrabi, H., 2006b. Dual role of deformation-induced geometrically necessary dislocations with respect to lattice plane misorientations and/or long-range internal stresses. Acta Mater. 54, 3417–3427. doi:10.1016/j.actamat.2006.03.047, Selected Papers from the Meeting “Micromechanics and Microstructure Evolution: Modeling, Simulation and Experiments” held in Madrid/Spain, 11–16 September 2005.

Neumann, P., 1983. Fatigue. North-Holland, Neumann, P.; Max-Planck-Inst. fur Eisenforschung GmbH, Dusseldorf, West Germany.

Nye, J.F., 1953. Some geometrical relations in dislocated crystals. Acta Metall. 1, 153–162. doi:10.1016/0001-6160(53)90054-6.

Overton, W.C., Gaffney, J., 1955. Temperature variation of the elastic constants of cubic elements. I. Copper. Phys. Rev. 98, 969–977. doi:10.1103/PhysRev.98.969.

Pantleon, W., 2008. Resolving the geometrically necessary dislocation content by conventional electron backscattering diffraction. Scr. Mater. 58, 994–997. doi:10.1016/j.scriptamat.2008.01.050.

Peirce, D., Asaro, R.J., Needleman, A., 1982. An analysis of nonuniform and localized deformation in ductile single crystals. Acta Metall. 30, 1087–1119. doi:10.1016/0001-6160(82)90005-0.

Roters, F., Eisenlohr, P., Hantcherli, L., Tjahjanto, D.D., Bieler, T.R., Raabe, D., 2010. Overview of constitutive laws, kinematics, homogenization and multiscale methods in crystal plasticity finite-element modeling: theory, experiments, applications. Acta Mater. 58, 1152–1211. doi:10.1016/j.actamat.2009.10.058.

Roters, F., Eisenlohr, P., Kords, C., Tjahjanto, D.D., Diehl, M., Raabe, D., 2012. DAMASK: the Düsseldorf advanced material simulation kit for studying crystal plasticity using an FE based or a spectral numerical solver. Procedia IUTAM 3, 3–10. doi:10.1016/j.piutam.2012.03.001.

Wilkens, M., Herz, K., Mughrabi, H., 1980. An X-Ray diffraction study of cyclically and of unidirectionally deformed copper single crystals. Z. Für Met. 71, 376–386.